RSC Advances

PAPER

View Article Online
View Journal | View Issue

Cite this: *RSC Adv.*, 2023, **13**, 21690

First-principles study on the structure and electronic properties of M_2CS_x (M = Sc, Ti, Y, Zr and Hf, x = 1, 2)†

Huaijin Zhu, [ab] Nianxiang Qiu,*[b] Gang Fang[b] and Shiyu Du *[bcde]

Two-dimensional (2D) transition metal carbides/nitrides, known as MXenes, have attracted extensive attention due to their rich elemental composition and diverse surface chemistry. In this study, the crystal structure, electronic, mechanical, and electronic transport properties of M_2CS_x (M = Sc, Ti, Y, Zr, and Hf, x = 1, 2) were investigated by density functional theory (DFT). Our results showed that the studied M_2CS_x except Y_2CS_2 are thermodynamically, dynamically, thermally, and mechanically stable. The p–d hybridization between the M-d state and the C/S-p state of M_2CS is stronger than that of the corresponding M_2CS_2. However, the antibonding state would appear near the Fermi level and thus reduce the thermal stability of the material due to the introduction of sulfur vacancies in the Y-free MXenes studied. In contrast, sulfur vacancies would significantly enhance the bonding states of Y–C and Y–S bonds and improve the stability of Y_2CS_x. This provides an explanation for the experimentally observed formation of non-stoichiometric $Ti_2CS_{1.2}$. The room-temperature electron mobilities of semiconductor Sc_2CS (Y_2CS) along the x and y directions were determined to be 232.59 (818.51) and 628.22 (552.55) $cm^2\ V^{-1}\ s^{-1}$, and the room-temperature hole mobilities are only 88.32 (1.64) and 61.75 (17.80) $cm^2\ V^{-1}\ s^{-1}$. This work is expected to provide theoretical insights for the preparation and application of S-terminated MXenes.

Received 19th May 2023
Accepted 30th June 2023

DOI: 10.1039/d3ra03340f

rsc.li/rsc-advances

1. Introduction

MXenes are a large family of two-dimensional (2D) transition metal carbides, nitrides, and carbonitrides with diverse structures, compositions, and surface chemistries, and have been widely used in many fields such as energy storage,[1,2] electronic devices,[3,4] sensors,[5,6] catalysts,[7,8] the environment,[9,10] and biomedicine.[11] MXenes are prepared by a top-down synthesis approach, that is, selective etching of A-layer elements from MAX phase precursors. The general formula of MXenes is $M_{n+1}X_nT_x$, where M represents the transition metal element (such as Sc, Ti, V), X is the C or N element, n can vary from 1 to 4, and T_x (x is a variable) indicates the surface group. Since the first MXene ($Ti_3C_2T_x$) was obtained by hydrofluoric acid etching in 2011,[12] more than 30 stoichiometric MXenes have been prepared and more than 100 compositions of MXenes have been predicted.[13] In addition, the surface termination of MXenes is dependent on the synthesis approach and MXene composition.[14–16] For example, the surface terminations of MXenes produced by wet chemical etching techniques are generally F, O, and OH.[15,17] The halogen-terminated MXenes can be synthesized by etching in Lewis acid $CuCl_2/CuBr_2/CuI_2$ molten salts.[18,19] These terminations can be substituted or eliminated by other functional groups such as S, Se, Te, NH groups through subsequent surface reactions, providing a new route to synthesize new MXenes that cannot be obtained by conventional Lewis acid etching.[16,20] The surface terminations of MXenes have a significant impact on the physical, chemical properties and structural stability of MXenes due to the overlapping of non-bonding valence electrons of transition metals through their low-energy electronic states.[21–23] Li *et al.* reported the I-terminated halogenated $Ti_3C_2I_2$ MXene cathode can activate and stabilize reversible I^0/I^+ redox couple in the I_2–Zn battery to achieve a high voltage plateau.[24] Superconductivity was first observed in Nb_2CT_x terminated with S, Se, or NH groups, while no superconducting transition was found for bare and O-terminated Nb_2C.[16] Some M_2CT_2 (T = O, OH or S)-based multifunctional sulfur cathodes were found to effectively suppress the shuttling effect and exhibit excellent cycle performance and high specific capacity in lithium–sulfur

[a]*Faculty of Electrical Engineering and Computer Science, Ningbo University, Ningbo, Zhejiang 351201, China*

[b]*Engineering Laboratory of Advanced Energy Materials, Ningbo Institute of Materials Technology and Engineering, Chinese Academy of Sciences, Ningbo, Zhejiang 315201, P. R. China. E-mail: qiunianxiang@nimte.ac.cn; dushiyu@nimte.ac.cn*

[c]*School of Materials Science and Engineering, China University of Petroleum (East China), Qingdao, 266580, China*

[d]*School of Computer Science, China University of Petroleum (East China), Qingdao, 266580, China*

[e]*Milky-Way Sustainable Energy Ltd, Zhuhai, China*

† Electronic supplementary information (ESI) available. See DOI: https://doi.org/10.1039/d3ra03340f

batteries.[25–27] Zhu *et al.* showed the O, OH and F groups on Zr_2CT_x can be seemingly exchanged with S groups through the proposed reaction in CS_2 solution.[28] A number of S-functionalized MXenes have been reported as electrode materials for potential metal ion batteries due to their lower diffusion barrier and higher storage capacity.[29–37] Luo *et al.* investigated the nitrogen reduction reaction (NRR) of Fe adsorbed on $Ti_3C_2O_2$ or N/F/P/S/Cl-doped $Ti_3C_2O_{2-x}$ MXene and found that F and S doping can reduce the energy barrier of the rate-determining step.[38] Bae *et al.* reported a new structural phase of Sc_2CO_2 containing C3 trimers converted from the hexagonal carbon of the typical trigonal MXene phase, with two very active anion electrons located in the voids between C3 trimers.[39] Additionally, Wang *et al.* demonstrated that the stable Sc_2CO_2 monolayer is an efficient NH_3 gas sensor with high selectivity, high sensitivity and low recovery time through analytical methods based on optical and/or electronic response.[40] In comparison, without directly considering the material stability, Hu *et al.* reported that Sc_2CS_2 could effectively capture the NH_3 and nicotine, while the Y_2CS_2 exhibits the extremely high sensitivity and selectivity towards NO.[41] Importantly, only non-stoichiometric chalcogen-terminated MXenes were observed in the experiment, *e.g.* $x = 1.2$ and 1.1 for Ti_2CS_x, and $Ti_3C_2S_x$, respectively,[16] despite the dynamical stability of stoichiometric M_2CS_2 (M = Sc, Ti, V, Cr, Fe, Y, Zr, Nb, Mo, Hf, Ta and W) and $Ti_3C_2S_2$ have been theoretically confirmed by the calculated phonon dispersions and *ab initio* molecular dynamics (AIMD) simulations.[27,29,42–49] To the best of our knowledge, the non-stoichiometric structures, underlying stability mechanisms and associated physical properties of S-terminated MXenes remain unclear.

In this study, the structural stability, electronic structure, mechanical and electronic transport properties of M_2CS_x (M = Sc, Ti, Y, Zr and Hf, $x = 1$, 2) were investigated using density functional theory (DFT). Our results showed that the calculated cohesive energies and bond lengths of the M–C and M–S bonds of M_2CS are smaller than those of the counterpart M_2CS_2 due to the more pronounced electron transfer and stronger p–d overlaying between M-d state and C/S-p state of M_2CS. In addition, due to the introduction of sulfur vacancy in the studied MXenes except Y_2CS_x, the antibonding state would appear near the Fermi level, reducing the thermal stability of the material. Furthermore, both Sc_2CS and Y_2CS were found to be a thermodynamically stable and dynamically stable semiconductors with appropriate carrier mobility. This work is expected to provide clues for the design and preparation of novel MXenes.

2. Computational details

All the first-principles calculations were carried out by using Vienna *Ab initio* Simulation Package (VASP). Projector augmented wave (PAW) method[50] was employed to describe the electron–core interactions and the generalized gradient approximation (GGA) of Perdew–Burke–Ernzerhof (PBE) was used to treat the exchange–correlation potential of valence electrons.[51] And the DFT-D3 method with Becke–Jonson damping were included in all calculations to account for the van der Waals (vdW) interaction.[52] The cutoff energy of plane waves was set to 500 eV. The Monkhorst–Pack meshes with $12 \times 12 \times 1$ and $9 \times 9 \times 1$ *k*-points were used to sample the Brillouin zone for the calculations of M_2CS_2 and M_2CS cells, respectively. A large vacuum thickness of 20 Å was used to avoid the spurious interaction between adjacent monolayers. The structures studied were fully optimized using conjugate gradient algorithm, and the energy and force convergences of 10^{-8} eV and 10^{-6} eV Å^{-1} were used for the calculations. In addition, density functional perturbation theory implemented in PHONOPY software was used to calculate phonon spectra to check the dynamical stability of the structures investigated.[53,54] And the $4 \times 4 \times 1$ supercell of M_2CS_2, $2 \times 2 \times 1$ supercell of M_2CS, plane wave with a cut-off energy of 650 eV and $4 \times 4 \times 1$ *k*-point meshes were used for force constant calculations. AIMD simulations were performed for 4 ps in NVT ensemble with a time step of 1.0 fs to assess thermal stability of M_2CS_x. The Nosé–Hoover thermostat was applied to control the temperature. In order to predict the electronic transport properties, band gap center E_{BGC} was calculated by using GGA-PBE functional and calibrated against vacuum level.[55] The band edge of MXene could be accurately evaluated as follows.[56–58]

$$E_{VBM} = E_{BGC} - \tfrac{1}{2}E_g \quad (1)$$

$$E_{CBM} = E_{BGC} + \tfrac{1}{2}E_g \quad (2)$$

Here E_g is the calculated band gap of MXene. Carrier mobility of 2D MXenes was studied based on the deformation potential theory according to eqn (3) because the carrier mobility of a 2D intrinsic inorganic semiconductor is mainly dominated by the phonon scattering.[59,60]

$$\mu_{2D} = \frac{2e\hbar^3 C_{2D}}{3k_B T E_i^2 |m^*|^2} \quad (3)$$

Here, $\hbar$ is the reduced Planck constant, T is the temperature, k_B is the Boltzmann's constant, e is the elementary charge. $m^* = \hbar^2/(\partial^2 E/\partial k^2)$ is the effective mass of charge, C_{2D} is the elastic modulus under the strain $\Delta a/a_0$ along the transport direction, determined by $C_{2D} = [\partial^2 E/\partial[\Delta a/a_0]^2]/S_0$, where E and S_0 is the total energy and the area of optimized supercell. And E_i represents the deformation potential constant of valence-band maximum for holes and conduction-band minimum for electrons, calculated by $E_i = \partial E_{edge}/\partial(\Delta a/a_0)$, where E_{edge} is the energy of *i*th energy band under a small compressive or tensile strain $\Delta a/a_0$ along the transport direction. All the structures were visualized by Materials Studio or VESTA3 software.[61]

3. Results and discussion

3.1. Crystal structure and stability of M_2CS_x

Four possible configurations for sulfur terminations of a M_2CS_2 crystal were considered in Fig. S1.† In order to assess the relative thermodynamic stabilities of the configurations studied, cohesive energy E_{coh} was calculated by

$$E_{coh} = [E_{tot}(M_2CS_x) - 2E(M) - E(C) - xE(S)]/(3 + x) \quad (4)$$

where $E_{tot}(M_2CS_x)$ is the total energy of M_2CS_x, $E(M)$, $E(C)$, and $E(S)$ are the energies of isolated M, C, and S atoms, respectively. From the calculated total energies of M_2CS_2 configurations in Table S1,† it is found that the sulfur layers on both sides of the most stable configuration of M_2CS_2 (M = Ti, Zr and Hf) (as shown in Fig. 1 and S1B†) are directly projected to the bottom metal layer, while in the most stable configuration of Sc_2CS_2 and Y_2CS_2, the sulfur atoms on one side are projected directly to the bottom metal atoms, while the sulfur atoms on the opposite side are projected directly to the carbon atoms in the middle layer (as shown in Fig. 1 and S1C†). Apparently, stable Ti_2CS_2, Zr_2CS_2, Hf_2CS_2 are symmetric type-A structures, while energetically preferred asymmetric type-B structures do exist in Sc_2CS_2 and Y_2CS_2. Interestingly, the stable configuration of the studied M_2CS_2 resembles the counterpart M_2CO_2.[40,62] However, Zhang *et al.*[42] reported that Sc_2CS_2 and Y_2CS_2 are actually stabilized in distortion variants of the asymmetric type-B phase depicted in Fig. 1 type-B. Therefore, the relative stability of the type-B phase and the distorted type-B phase of Sc_2CS_2 and Y_2CS_2 was compared, and the results are displayed in Table S2 and Fig. S2.† Noteworthily, the dipole-corrected total energies of type-B Sc_2CS_2 and Y_2CS_2 calculated in this study are larger than those reported by Zhang *et al.*[42] probably due to the higher convergence criteria used in this study. And the distorted structures of type-B Sc_2CS_2 and Y_2CS_2 were optimized back to the type-B phase with the structural symmetry switched off, resulting in their almost identical total energies. This is probably due to the fact that the imaginary phonon modes around the high symmetry point *K* that lead to the distortion disappear in our calculated phonon spectra (Fig. S6†). This similar distorted structure was also found in transition metal dichalcogenides, but it was determined as a transient state between the 2H phase and the T_d phase.[63] Therefore, further exploration of this possible distorted phase of type-B Sc_2CS_2 and Y_2CS_2 is beyond the scope of this study.

On the basis of the most stable structure of M_2CS_2, all possible configurations of M_2CS were constructed by $2 \times 2 \times 1$ cell expansion and removal of half of the S terminations, which were done by disorder code.[64] There are six possible configures for Ti_2CS, Zr_2CS, Hf_2CS as depicted in Fig. S3,† and nine possible configures for Sc_2CS, Y_2CS as shown in Fig. S4.† Interestingly, it can be seen from Tables S3 and S4† that the S groups on both sides of all studied M_2CS are preferentially arranged in stripes, as shown in Fig. S3 DEF and S4 DEF.† That is, the strip-like S groups on both sides of M_2CS_2 are removed in turn, so that the number of S atoms removed on both sides is identical. More importantly, among all the arrangements of stripe-like S terminations, the stripe-like S terminations on both sides of M_2CS are preferentially parallel and the distance between the two stripe-like S groups is the shortest in the *xy* plane as displayed in Fig. 1 type-C or S3D and S4F.† This can maintain the crystalline structure of M_2CS_2 to the greatest extent. Furthermore, it is evident from Table S3† that it is most energetically unfavorable to completely remove the S atoms on one side of the symmetric type-A M_2CS_2 to expose the MXene, but this is not necessarily the case for the asymmetric type-B M_2CS_2. As with the symmetric type-A phase, it is most energetically unfavorable to remove all the S atoms projected to the bottom M atoms of the asymmetric type-B M_2CS_2 (Fig. S4A†). But it can be seen from Table S4† that removing all S atoms projected to C atoms (Fig. S4I†) is easier than removing 1 S atom projected to the bottom M atom and 3 S atoms projected to the C atoms (Fig. S4G and H†). Importantly, considering the small energy differences among the three configurations A, B, and C of the stoichiometric M_2CS_2 in Table S1,† the most stable non-stoichiometric M_2CS configurations derived from these three configurations were also investigated and presented in Fig. S5,† and their corresponding calculated energies are listed in Table S5.† It is evident from Table S5† that the total energy of the most stable configuration of M_2CS (M = Sc, Ti, Y, Zr, and Hf) with stripe-like S terminations derived from symmetric type-A M_2CS_2 (Fig. 1 and S1B†) is the smallest, indicating that regardless of the stable configuration of M_2CS_2, the stripe-like S terminations

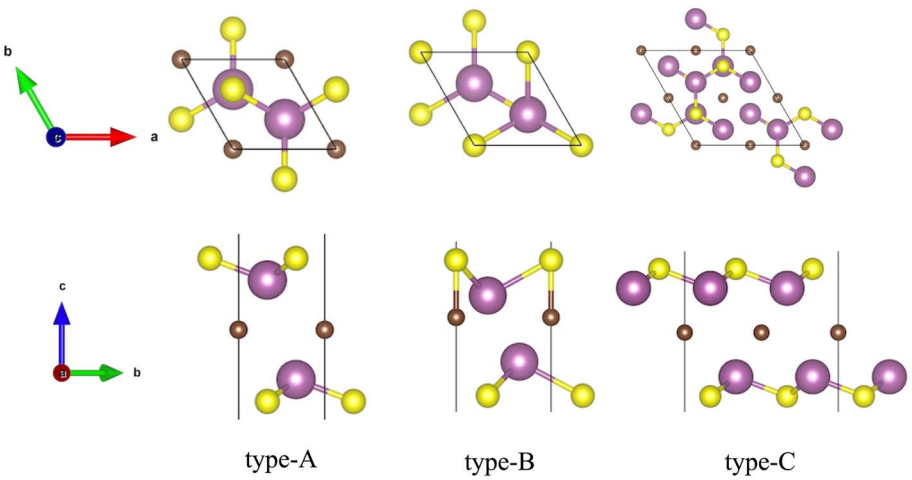

Fig. 1 The optimized most stable configurations of M_2CS_x (M = Sc, Ti, Y, Zr and Hf, $x = 1, 2$). Type-A: the top and side views of the most stable configurations of M_2CS_2 (M = Ti, Zr and Hf), type-B: the top and side views of the most stable configurations of Sc_2CS_2 and Y_2CS_2, type-C: the top and side views of the most stable configurations of M_2CS (M = Sc, Ti, Y, Zr and Hf).

Table 1 The calculated Lattice constant (Å), space group, cohesive energy E_{coh} (eV per atom) and bond lengths (Å) of M–S and M–C bonds of M_2CS_x (M = Sc, Ti, Y, Zr and Hf, x = 1, 2)

	Lattice constant	Bond length					Lattice constant	Bond length			
Material	a	M–S	M–C	Space group	E_{coh}	Material	a	M–S	M–C	Space group	E_{coh}
Sc_2CS_2	3.76	2.484/2.459	2.293/2.650	$P3m1$	−6.03	Sc_2CS	6.82	2.474	2.253	$P2_1/m$	−6.30
Ti_2CS_2	3.16	2.395	2.189	$P3m1$	−6.70	Ti_2CS	6.17	2.358	2.093	$P2_1/m$	−7.00
Y_2CS_2	4.17	2.628/2.605	2.485/2.877	$P3m1$	−6.52	Y_2CS	7.37	2.656	2.429	$P2_1/m$	−6.62
Zr_2CS_2	3.44	2.531	2.394	$P3m1$	−8.13	Zr_2CS	6.64	2.508	2.278	$P2_1/m$	−8.15
Hf_2CS_2	3.40	2.508	2.366	$P3m1$	−7.92	Hf_2CS	6.54	2.477	2.260	$P2_1/m$	−8.14

Table 2 Loewdin atomic charge of M_2CS_x (M = Sc, Ti, Y, Zr and Hf, x = 1, 2)

Material	C	S	M	Material	C	S	M
Sc_2CS_2	−1.53	−0.31/−0.85	1.32/1.46	Sc_2CS	−1.95	−0.94	1.45/1.48
Ti_2CS_2	−1.73	−0.56	1.42	Ti_2CS	−1.90	−0.78	1.30/1.38
Y_2CS_2	−0.85	−0.43/−0.10	0.75/0.63	Y_2CS	−0.91	−0.46	0.67/0.70
Zr_2CS_2	−1.59	−0.54	1.36	Zr_2CS	−1.63	−0.69	1.28/1.30
Hf_2CS_2	−1.08	−0.31	0.85	Hf_2CS	−1.02	−0.42	0.70/0.73

of M_2CS tend to be located on top of the underlying metal layer as shown in Fig. 1 type-C.

The calculated lattice constants, cohesive energies, space groups and bond lengths of M–S and M–C bonds of the most stable configurations of M_2CS_2 and M_2CS studied are shown in Table 1. For all M_2CS_x (x = 1 or 2) studied, the cohesive energy of M_2CS_x is negative, compared to the respective E_{coh} values of −6.38 and −5.06 eV per atom for Sc_2CO_2 (ref. 65) and Ti_2CO_2,[66] which indicates that they are thermodynamically stable to the isolated constituent atoms. The space group of the M_2CS_2 studied is $P3m1$, consistent with the experimental observations of traditional stoichiometric MXenes,[16] while the space group of M_2CS (M = Sc, Ti, Y, Zr, and Hf) is $P2_1/m$. The lattice parameter a = 3.16 Å of Ti_2CS_2 and the lattice constant a = 6.17 Å of Ti_2CS are close to the experimentally observed a value of 3.21 Å for Ti_2CS.[16] And the lattice constants of M_2CS_2 (M = Sc, Ti, Zr and Hf) are slightly larger than those of the corresponding M_2CO_2 (*i.e.* 3.41, 3.04, 3.31 and 3.27 Å for Sc_2CO_2, Ti_2CO_2, Zr_2CO_2 and Hf_2CO_2)[67] due to the weaker M–S bond relative to the M–O bond.

Clearly, it can be seen that the lattice constant of Y_2CS_x is the largest among the studied M_2CS_x with the same formula due to the weak interatomic bonding of Y–C and Y–S, which will be explained in detail in Section 3.2. The calculated Ti–C bond length of 2.09 Å and Ti–S bond length of 2.36 Å for the Ti_2CS are in good agreement with the experimentally observed Ti–C and Ti–S bond lengths of 2.14 Å and 2.41 Å.[16] Importantly, the M–C and M–S bond lengths of the M_2CS_2 studied are longer than those of the counterpart M_2CS. And the calculated E_{coh} of the M_2CS_2 studied are greater than those of the counterpart M_2CS. In addition, it can be found from Table 2 that the net negative charge of S and C atoms of the M_2CS_2 studied are smaller than those of the corresponding M_2CS, which indicates that more electrons are transferred from the M atom to the C and S atoms of the M_2CS than the corresponding M_2CS_2. The significant charge transfer can also be visually observed from the charge density difference in Fig. S6.† This confirms that the M–C and M–S bonds of M_2CS are stronger than the corresponding M_2CS_2.

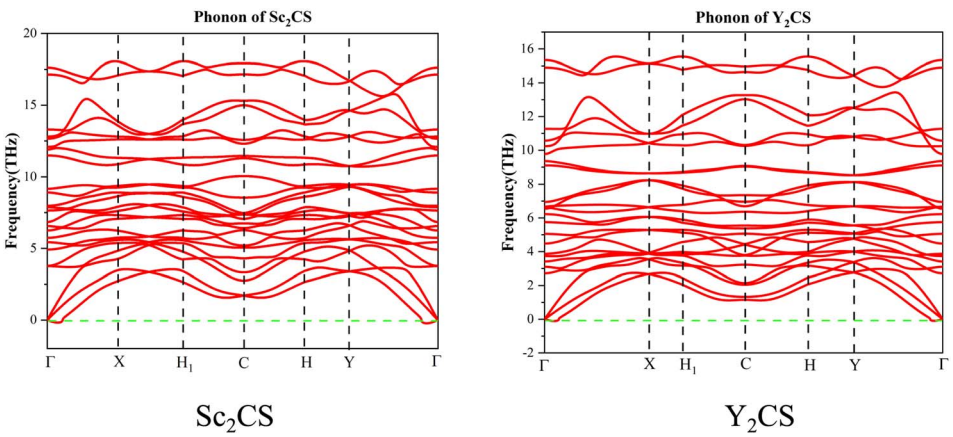

Fig. 2 The calculated phonon dispersions of the Sc_2CS and Y_2CS.

In order to further check the dynamical stability of MXenes, the phonon dispersion curves of M_2CS_x were calculated. It is worth mentioning that small imaginary frequencies near the Γ point are often observed in the calculated phonon spectra of 2D systems, which could be caused by numerical noise owing to the vacuum region.[68–70] As shown in Fig. 2 and S6,† almost no imaginary frequency is observed in the phonon dispersions of M_2CS (M = Sc, Ti, Zr, and Y), and some small negative frequencies near the Γ point appear in the phonon dispersion curves of M_2CS_2 (M = Sc, Ti, Zr, and Hf) and Hf_2CS. This is an indication of dynamic stabilities of M_2CS_x studied except Y_2CS_2, consistent with the fact that Ti_2CS was found in experiments.[16] As a comparison, the exception Y_2CS_2 shows significant imaginary frequencies in the phonon dispersion, consistent with previously reported results by Zhang *et al.*[42] and Li *et al.*,[68] which is a sign that the formation of the Y_2CS_2 MXene probably needs more inspection from experiments. Then, AIMD simulations were performed to further evaluate the dynamical and thermal stabilities of the M_2CS_x studied as displayed in Fig. 3. There is no broken M–C and M–S bonds or obvious structural reconstruction within a simulation of 4 ps at 300 K for the M_2CS (M = Sc, Y, and Zr) and even at 900 K for the M_2CS_2 (M = Sc, Ti, Zr, and Hf) and Hf_2CS, manifesting the good thermal stability of these S-terminated MXenes. While for Ti_2CS, at 300 K, a structural reconstruction of part of the S-terminations moving from the top of bottom metal to the top of the carbon layer is observed, indicating that the strip-like S-terminations of Ti_2CS are temperature-sensitive. In contrast, Y_2CS_2 exhibits a pronounced destruction within 4 ps simulations at 300 K, which can be regarded as evidence of poor thermal stability, consistent with the observation of significant imaginary frequency. From the above analysis, it can be seen that the studied M_2CS_x except Y_2CS_2 has good dynamical and thermal stability, and it is particularly noted that the strip-shaped S functional groups of Ti_2CS are temperature sensitive and easily disturbed. Chen *et al.*[71] demonstrated that the stabilization of a certain surface configuration of MXene was the statistical average of the adsorption and desorption of surface functional groups. Thus, the total energy of a certain surface configuration is a function of the chemical potential of the functional group. When the chemical potential of the S functional group is high, close to its upper limit (*i.e.*, the chemical potential of elemental S_8), the stoichiometric M_2CS_2 is the thermodynamically most favorable configuration under such condition. As a comparison, when the chemical potential of the S functional group is small, the non-stoichiometric M_2CS_x may be the thermodynamically preferred configuration, and even M_2CS_x would decompose into bare M_2C and elemental sulfur or sulfide. In the experimental preparation,[16,20] sulfur-functionalized MXene was obtained by functional group substitution of halogen-functionalized MXene by Li_2S or intercalation of bare MXene by FeS or CuS. Under such preparation conditions, the chemical potential of the S functional group is generally lower, which is more conducive to the formation of non-stoichiometric S-functionalized MXenes, which may be the reason why no stoichiometric S-functionalized MXenes were observed experimentally. Zhu *et al.*[28] theoretically clarified the feasibility of interconversion of Zr_2CO_2 and excess CS_2 to Zr_2CS_2 under the release of COS.

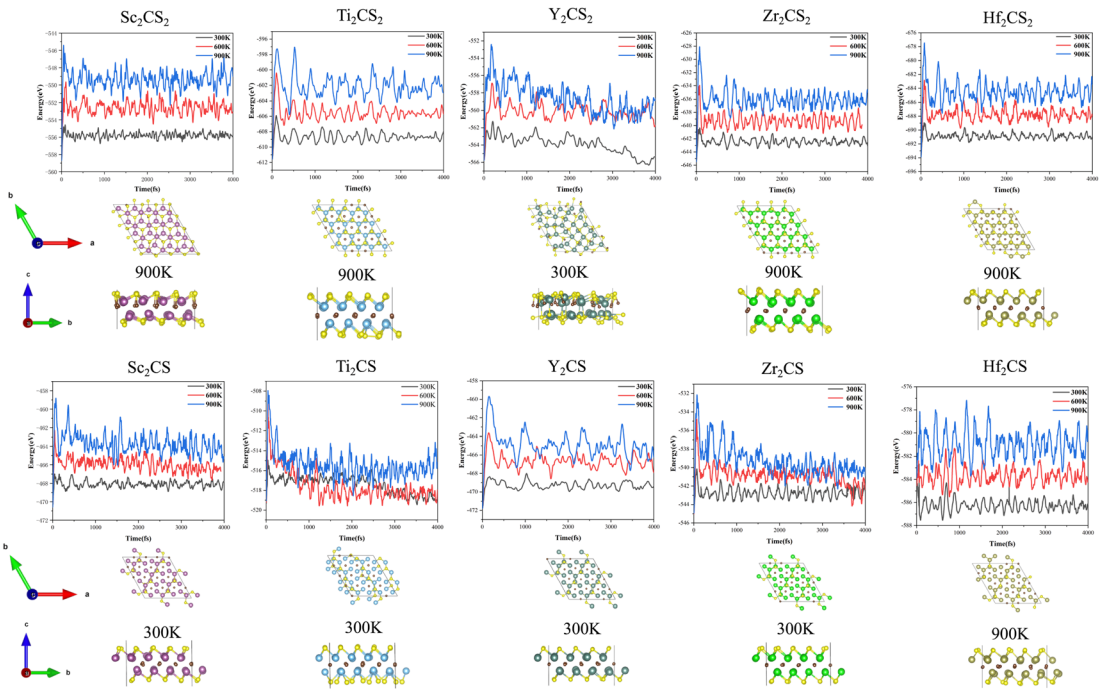

Fig. 3 Free energy fluctuations with respect to time at 300 K, 600 K and 900 K in AIMD simulations for M_2CS_x (M = Sc, Ti, Y, Zr, and Hf, $x = 1, 2$), and the obtained structures of M_2CS_x after AIMD simulations at specific temperature. The specified temperature in the figure is the highest temperature at which the structure can be kept stable among the three temperatures studied. Noteworthily, the reconstruction of the surface functional groups of Ti_2CS and the pronounced destruction of Y_2CS_2 were observed at the lowest temperature studied, 300 K.

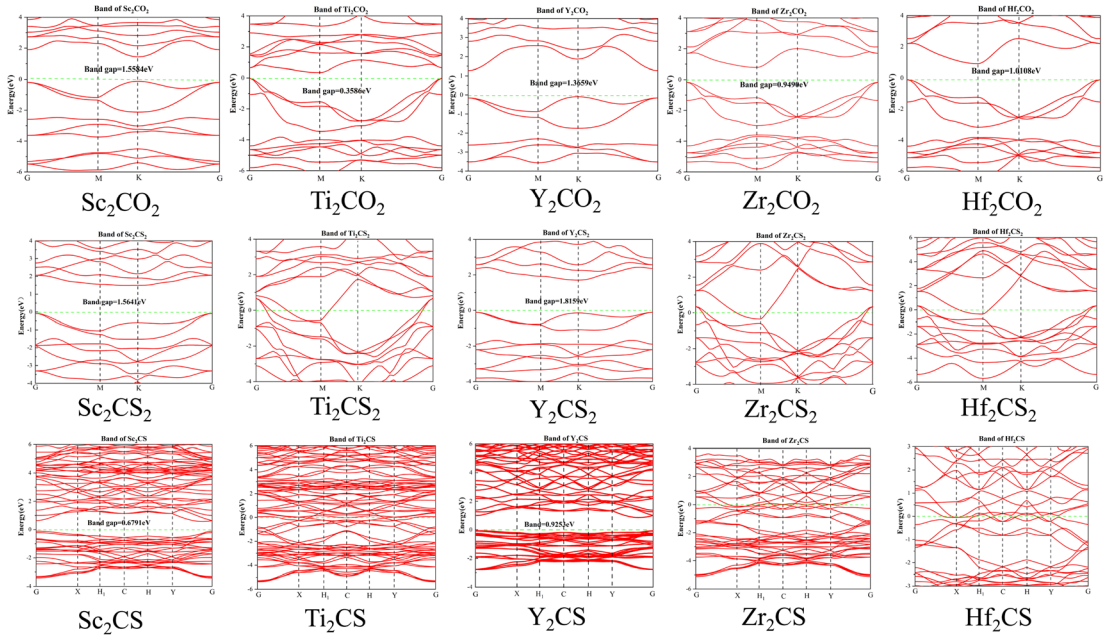

Fig. 4 The band structures of M_2CS_x (M = Sc, Ti, Y, Zr, and Hf, $x = 1, 2$) together with the corresponding M_2CO_2. The bandgaps of semiconductor materials are shown in the figure.

Therefore, under suitable experimental conditions with high chemical potential of the functional group S, stoichiometric S-functionalized MXenes can be prepared.

3.2. Electronic structure and bonding mechanism of M_2CS_x

In order to explore the electronic structures of the S-functionalized M_2CS_x (M = Sc, Ti, Y, Zr, and Hf, $x = 1, 2$) studied, the calculated electronic band structures of M_2CS_x as well as the corresponding M_2CO_2 for comparison are presented in Fig. 4. It can be readily found that the studied M_2CO_2 are all indirect bandgap semiconductors, in good accordance with the previous reported results.[40,67] Interestingly, four sulfur-terminated MXenes Sc_2CS_2, Y_2CS_2, Sc_2CS, and Y_2CS were identified as indirect bandgap semiconductors with bandgaps of 1.56, 1.85, 0.68, and 0.92 eV, respectively, which are larger than the bandgaps of 1.56 and 1.37 eV for the counterparts Sc_2CO_2 and Y_2CO_2. In contrast, the energy bands of the studied M_2CS_x (M = Ti, Zr, and Hf, $x = 1, 2$) crossing Fermi level exhibit the metallic-like features due to the presence of nonbonding M-d states at the Fermi level in Fig. 5. Since the traditional PBE functional generally underestimates the band gap of the material, the band gap of the sulfur-terminated MXene was corrected

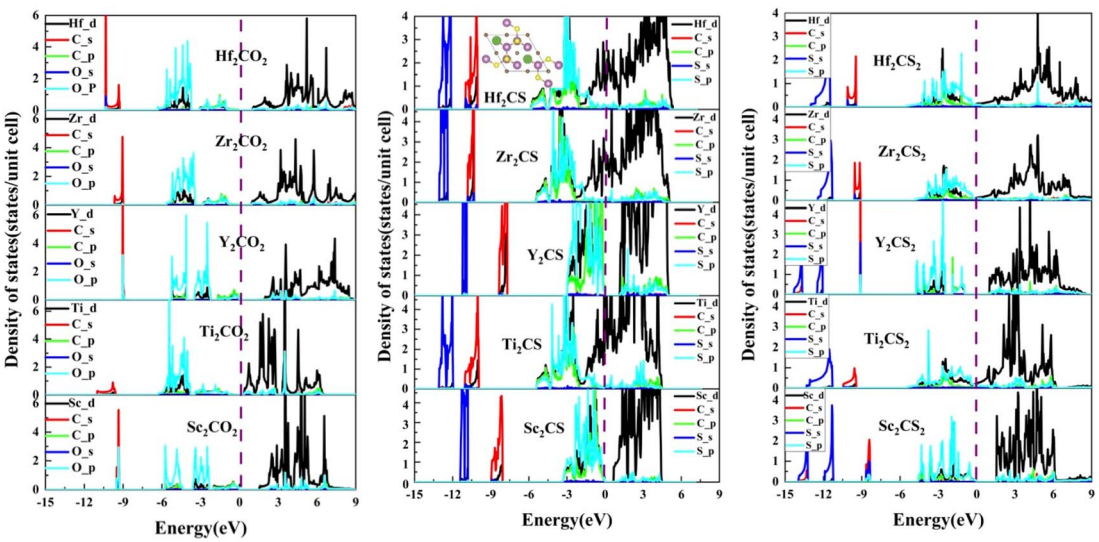

Fig. 5 The projected density of states (PDOS) of the M_2CS_x (M = Sc, Ti, Y, Zr, and Hf, $x = 1, 2$) as well as the corresponding M_2CO_2. The green spheres in the insert indicate S vacancies. The black curves represent M-d orbitals, the red and green curves represent C-s and -p orbitals, respectively, and the blue and cyan curves represent S-s and -p orbitals, respectively.

by the HSE06 functional.[72] After HSE06 correction, the band gaps of Sc_2CS_2, Y_2CS_2, Sc_2CS and Y_2CS were increased to 2.54, 2.75, 1.43 and 1.69 eV, respectively. Their suitable bandgap endows them with great potential as electronic devices. Cautious inspection from the calculated band gaps of M_2CS_x (M = Sc and Y, $x = 1, 2$) reveals that sulfur vacancy defects increase the unbonded electrons near the Fermi level of metal atoms on the MXene surface leading to the attenuation of the band gap.

In order to study the underlying bonding mechanism of the studied M_2CS_x, the projected density of states (PDOS) of M_2CS_x together with the corresponding M_2CO_2 for comparison were investigated as depicted in Fig. 5. For all MXenes studied, the electronic states above the Fermi level are dominated by nonbonding t_{2g} states and antibonding e_g^* states of the M-d orbital. Noteworthily, the S-p state of M_2CS_x overlaps with the M-d state in the energy range from −4.5 eV to 0 eV, while the O-p state of M_2CO_2 hybridizes with the M-d state around −6 to −2 eV, which is an implication of the stronger M–O bond than M–S bond. Resembling the corresponding M_2CO_2, due to the splitting of the 5-fold degenerate M-d orbitals of M_2CS_2 in the octahedral crystal field of MX_6, 5 hybridization peaks of the S-p state are observed, which are more conspicuous in Y_2CS_2 and Sc_2CS_2, but this phenomenon disappears in M_2CS due to the presence of S vacancies. In particular, the p–d hybridization peaks between S and Y of Y_2CS_2 are very localized, reflecting the weak nature of the Y–S bond, which are significantly improved in Y_2CS. More importantly, the hybridization peaks between the M-d orbital and the C-p or S-p orbital of M_2CS are remarkably higher than those of the corresponding M_2CS_2, which can be regarded as evidence that the M–C and M–S bonds in M_2CS are stronger than those in M_2CS_2.

To explore bonding/antibonding states of bonds of the studied M_2CS_x (M = Sc, Ti, Y, Zr, and Hf, $x = 1, 2$), the projected crystal orbital Hamilton population (*p*COHP) was calculated using the LOBSTER program,[73] as shown in Fig. 6. A positive value of −*p*COHP indicates a bonding state, and a negative value indicates an antibonding state. The hybridization between M and C and between M and S of the investigated M_2CS is stronger than that of the corresponding M_2CS_2 (seen in Fig. 5) leading to greater splitting of bonding and antibonding states in Fig. 6, *i.e.* farther away from the Fermi energy level, consistent with the reported results of Ti_2CO_2.[74] However, the introduction of sulfur vacancies will increase the non-bonding e_g states of the metal d orbitals, thereby making the antibonding states appear near the Fermi level and significantly reducing the thermal stability of the material, consistent with the AIMD simulation results. Especially, both the bonding and antibonding states of the Y–S bond of Y_2CS_2 are very small, again manifesting a weak Y–S bond, leading to the largest lattice constant of Y_2CS_2 among all studied MXenes. On the contrary, the bonding states of the Y–C and Y–S bonds of Y_2CS are very obviously enhanced, significantly improving the stability of Y_2CS_x. Consequently, the d–p hybridization between the metal and C/S atoms of M_2CS is significantly higher than that of the corresponding M_2CS_2, resulting in stronger M–C and M–S bonds in M_2CS than in M_2CS_2. However, due to the introduction of sulfur vacancies in other studied MXenes except Y_2CS_x, the antibonding state would appear near the Fermi level, reducing the thermal stability of the material. On the contrary, sulfur

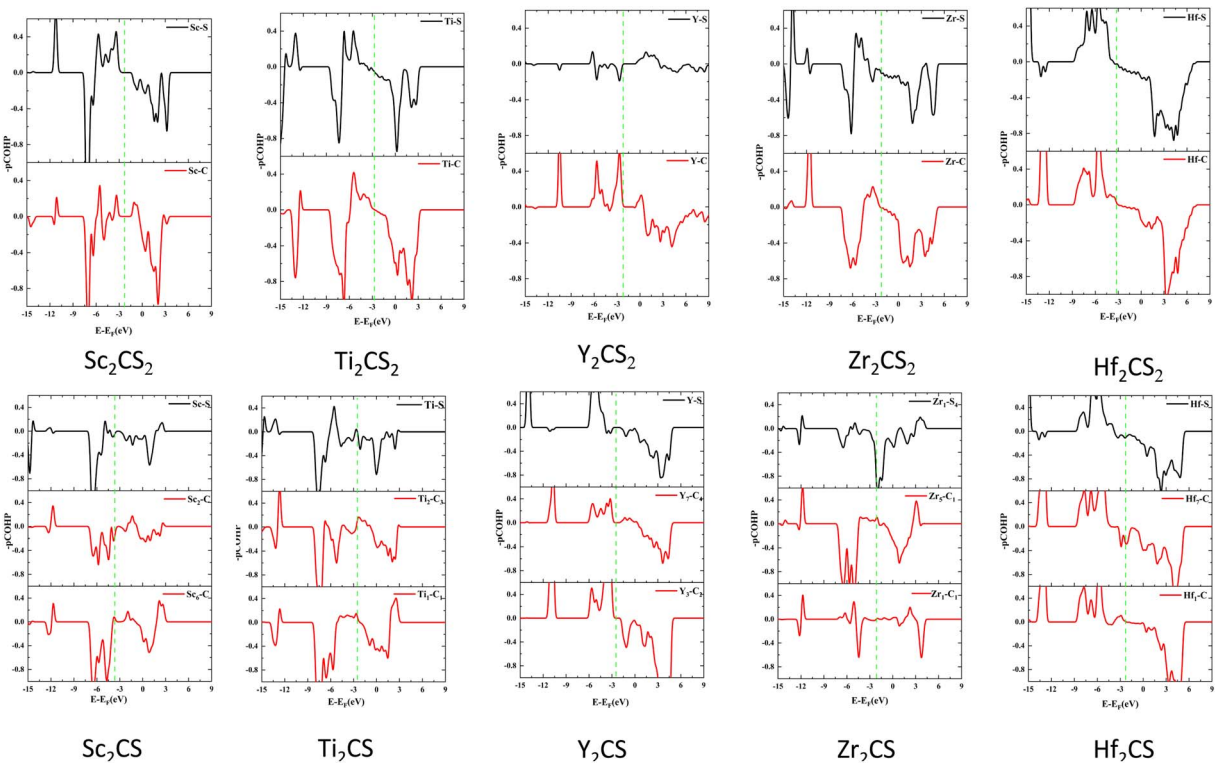

Fig. 6 The calculated COHP curves of M_2CS_x (M = Sc, Ti, Y, Zr, and Hf, $x = 1, 2$). The vertical green dotted line represents the Fermi level.

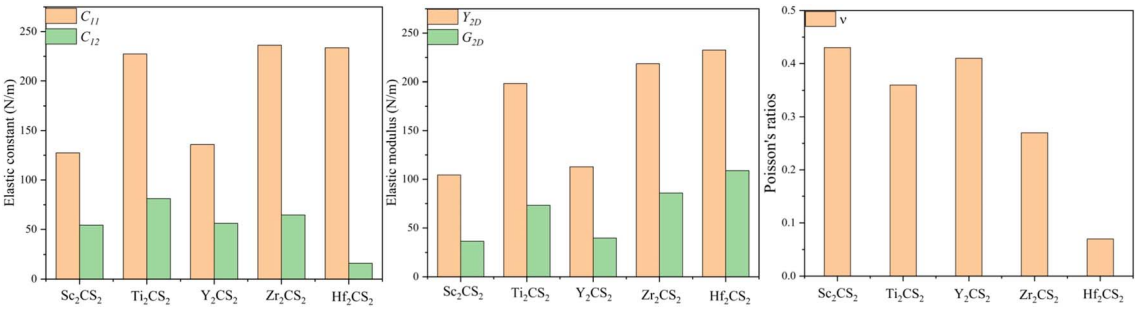

Fig. 7 The elastic constants C_{11}, C_{12}, in-plane Young's moduli Y_{2D}, in-plane shear moduli G_{2D} (in N m^{-1}), and Poisson's ratios v of the M_2CS_2 MXenes studied.

vacancies would significantly enhance the bonding states of Y–C and Y–S bonds and improve the stability of Y_2CS_x.

3.3. Mechanical properties

The fabrication of 2D crystal-based electronics generally requires high in-plane stiffness to avoid curling and obtain free-standing membranes. Therefore, the mechanical properties of M_2CS_x (M = Sc, Ti, Y, Zr, and Hf, x = 1, 2) were investigated by examining their elastic constants. Elastic constants C_{ij} of 2D crystal can be obtained by the first-principles energy-strain method, which is based on the energy variant by applying a small strain ε onto the equilibrium structure. Subsequently, the in-plane Young's modulus Y_{2D}, in-plane shear modulus G_{2D} (in N m^{-1}), and Poisson's ratios v can be obtained by eqn (5)–(7)[70]

$$Y_{2D} = (C_{11}^2 - C_{12}^2/C_{11}) \quad (5)$$

$$G_{2D} = 1/2(C_{11} - C_{12}) \quad (6)$$

$$v = C_{12}/C_{11} \quad (7)$$

The 2D crystal structure is determined to be mechanically stable when all elastic constants satisfy the well-known Born–Huang criteria:[75] For a trigonal M_2CS_2 structure: $C_{11} > 0$, $C_{11} > |C_{12}|$, $C_{66} > 0$, and for a monoclinic M_2CS structure: $C_{11} > 0$, $C_{11}C_{12} > C_{12}C_{12}$, $C_{ij} > 0$. The calculated elastic constants of M_2CS_x (M = Sc, Ti, Y, Zr, and Hf, x = 1, 2) in Fig. 7 and Table 3 meet the mechanical stability criteria, indicating they are mechanically stable under ambient conditions. It is evident that all the in-plane stiffnesses of Sc_2CS_x and Y_2CS_x are much smaller than those of the M_2CS_x (M = Ti, Zr, and Hf) probably due to the smaller cohesive energies of Sc_2CS_x and Y_2CS_x relative to M_2CS_x (M = Ti, Zr, and Hf). And the maximum Y_{2D} and G_{2D} values of Sc_2CS and Y_2CS are larger than those of Sc_2CS_2 and Y_2CS_2, respectively, due to the stronger M–C and M–S bonds of M_2CS compared with M_2CS_2, while M_2CS_x (M = Ti, Zr, and Hf) show the opposite trend, which may be caused by the anti-bonding states of M–C bond occurring at the Fermi level of M_2CS (Fig. 6). The in-plane Young's modulus and in-plane shear modulus of 104.39 and 36.61 N m^{-1} for Sc_2CS_2 is the smallest among all the studied M_2CS_2, which are smaller than those of Sc_2CO_2.[67] Noteworthily, the calculated in-plane Young's moduli of the semiconductors Sc_2CS and Y_2CS are 125.06–140.35 and 82.77–125.34 N m^{-1}, respectively, which are comparable to those of $MoSe_2$ (125 N m^{-1}) and MoS_2 (168 N m^{-1}),[76] indicating that Sc_2CS and Y_2CS monolayer have good mechanical properties. And it is further found that their Poisson's ratios v are all within 0.3. Since the low Poisson's ratio is favorable for the application of MXenes in flexible device materials,[66] Sc_2CS and Y_2CS MXenes have the potential to be used as flexible electronic devices.

3.4. Carrier mobility of nonstoichiometric Sc_2CS and Y_2CS MXenes

Carrier mobility is an important physical quantity to measure the performance of electronic devices. The orthorhombic Sc_2CS and Y_2CS supercell was adopted to calculate the carrier mobility according to deformation potential theory. As shown in Fig. 8a and e, the valence band maximum (VBM) of Sc_2CS and Y_2CS at Γ point is observed while the conduction band minimum (CBM) appears at the K point along Γ–X direction in the electronic band structure of nonstoichiometric Sc_2CS and Y_2CS. As an important band structure-derived property, effective masses of

Table 3 The elastic constants C_{11}, C_{12}, in-plane Young's moduli Y_{2D}, in-plane shear moduli G_{2D} (in N m^{-1}), and Poisson's ratios v of the M_2CS MXenes studied

	C_{11}	C_{12}	Y_{2D} (min)	Y_{2D} (max)	G_{2D} (min)	G_{2D} (max)	v (min)	v (max)
Sc_2CS	138.95	42.61	125.06	140.35	50.16	50.99	0.27	0.31
Ti_2CS	194.49	55.80	175.98	196.30	70.03	75.02	0.23	0.30
Y_2CS	120.15	38.14	82.77	125.34	36.05	43.62	0.25	0.49
Zr_2CS	196.50	56.84	176.01	194.32	69.85	74.81	0.24	0.31
Hf_2CS	217.28	58.13	197.22	210.13	79.22	82.62	0.24	0.28

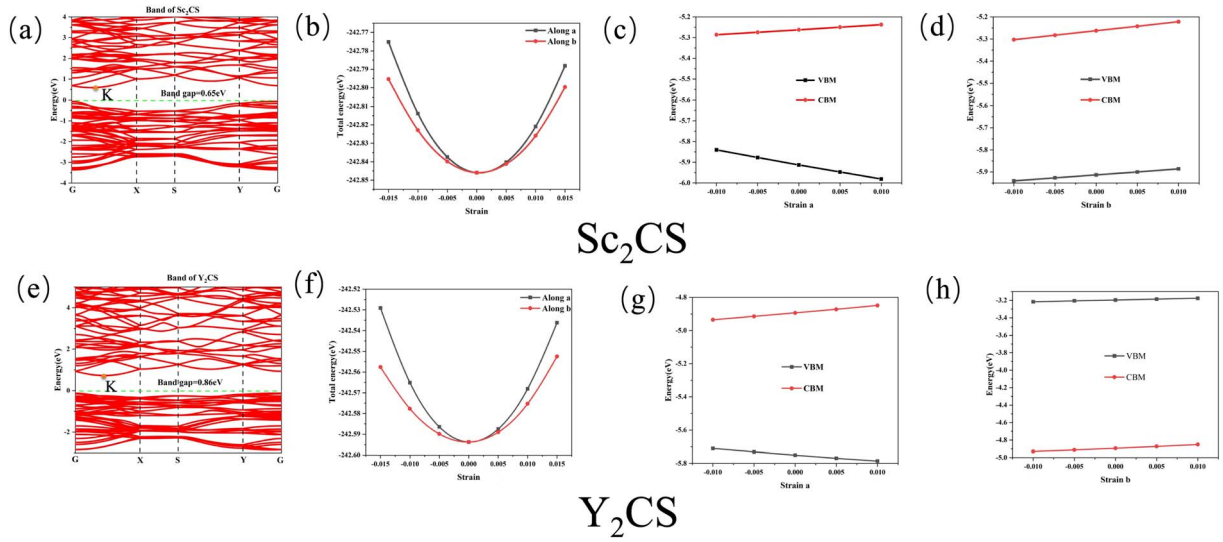

Fig. 8 (a) and (e) The calculated band structure of Sc_2CS and Y_2CS monolayer in the orthogonal supercell, (b) and (f) energy–strain relationship along x (Γ–X) and y (Γ–Y) directions of Sc_2CS and Y_2CS supercell, and (c), (d), (g) and (h) band edges as a function of strain along x and y directions of Sc_2CS and Y_2CS supercell, respectively.

Table 4 The calculated carrier mobilities of nonstoichiometric Sc_2CS and Y_2CS

	Carrier type	Direction	C_{2D} (J m^{-2})	E_1 (eV)	m^* (m_e)	μ (cm^2 V^{-1} s^{-1})	τ (fs)
Sc_2CS	Electron	x	111.98	7.03	0.70	232.59	92.58
		y	84.33	4.06	0.64	628.22	228.62
	Hole	x	111.98	2.42	3.30	88.32	165.72
		y	84.33	4.06	2.04	61.75	71.72
Y_2CS	Electron	x	91.02	4.30	0.55	818.51	255.98
		y	57.66	3.95	0.58	552.55	182.23
	Hole	x	91.02	3.76	14.04	1.64	13.11
		y	57.66	2.01	6.35	17.80	64.28

electrons at K point and holes at Γ point of Sc_2CS and Y_2CS were calculated and shown in Table 4. For both Sc_2CS and Y_2CS, it can be readily found that the effective hole mass is much larger than the effective electron mass, suggesting that electrons can have higher mobility than holes under an external electric field due to the much smaller effective mass. Interestingly, the effective electron mass and effective hole mass of Sc_2CS along x direction are larger than those along y direction, respectively, and the effective hole mass of Y_2CS material also shows the same trend, showing effective mass anisotropy. In detail, the effective mass of electrons of Sc_2CS along x direction is $0.70m_e$, which is 9.4% larger than that along y direction, while the effective mass of holes along x direction ($3.30m_e$) is 61.8% larger than that along y direction. In comparison, for Y_2CS, the effective electron masses along the x and y directions are almost equal, but the effective hole mass along the x direction is 1.21 times larger than along the x direction. Besides the effective mass, the deformation potential constant E_l and elastic modulus C_{2D} of Sc_2CS and Y_2CS MXene were also calculated. The C_{2D} value of electrons and holes of Sc_2CS and Y_2CS along x direction is 111.98 and 91.02 J m^{-2}, which is 32.8% and 57.9% larger than those along the y direction, respectively. Additionally, the E_l values (7.03 eV) of holes at Γ point of Sc_2CS along x direction is 1.73 times that along y direction, while the E_l of electrons at K point along the x direction is only 0.60 times that along the y direction. And the deformation potential constants of holes at Γ point of Y_2CS along x and y directions are 4.30 and 3.76 eV, which are 0.35 and 1.75 eV larger than those of electrons at K point along x and y directions, respectively.

Therefore, according to eqn (3), the electron mobilities and hole mobilities of Sc_2CS and Y_2CS are predicted and summarized in Table 4. The room-temperature electron mobilities of Sc_2CS along the x and y directions were determined to be 232.59 and 628.22 cm^2 V^{-1} s^{-1}, respectively, compared with the room-temperature hole mobilities of only 88.32 and 61.75 cm^2 V^{-1} s^{-1} along the x and y directions. That is, the electron mobilities along the x and y directions are about 2.63 and 10.17 times that of the holes, respectively, due to the large difference in effective mass, which exhibits pronounced anisotropy. Resembling the charge transport of Sc_2CS, the electron mobilities of Y_2CS along the x and y directions (818.51 and 552.55 cm^2 V^{-1} s^{-1}, respectively) are 498 and 30 times higher than the hole mobilities

along the x and y directions. Therefore, it can be said that the charge transport of Sc_2CS is predominated by electron, which is different from our recently reported Sc_2CO_2 with similar electron and hole mobilities.[40] In addition, the predicted carrier mobility of non-stoichiometric Sc_2CS is much higher than that of MoS_2 monolayer,[77] but much smaller than that of Sc_2CO_2 (ref. 40) due to defect scattering caused by sulfur vacancies. Therefore, the structurally stable Sc_2CS and Y_2CS with suitable carrier mobility and mechanical properties may serve as an excellent nanoelectronic material.

4. Conclusion

In this study, the structural stability, electronic structure, elastic and charge transport properties of M_2CS_x (M = Sc, Ti, Y, Zr, and Hf, x = 1, 2) were studied by using first-principles density functional theory. The studied M_2CS_x except Y_2CS_2 were determined to be thermodynamically, dynamically, thermally, and mechanically stable, suggesting that these S-functionalized MXenes can be successfully prepared. In contrast to all studied M_2CO_2 being indirect bandgap semiconductors, only four S-terminated MXenes (Sc_2CS_2, Y_2CS_2, Sc_2CS, and Y_2CS) were identified as indirect bandgap semiconductors. The p–d hybridization between the M-d state and the S/C-p state of M_2CS is stronger than that of M_2CS_2, indicating that the bonding strength of the M–C/S bond in M_2CS is stronger. However, due to the introduction of sulfur vacancies in the Y-free MXene, an antibonding state would occur near the Fermi level, thereby reducing the thermal stability of the material. On the contrary, the sulfur vacancies would significantly enhance the bonding state of Y–C and Y–S bonds and improve the stability of Y_2CS_x. These provides an explanation for the experimentally observed formation of non-stoichiometric M_2CS_x. And the room-temperature electron mobilities of Sc_2CS (Y_2CS) along the x and y directions were determined to be 232.59 (818.51) and 628.22 (552.55) $cm^2\ V^{-1}\ s^{-1}$, compared with the room-temperature hole mobilities of only 88.32 (1.64) and 61.75 (17.80) $cm^2\ V^{-1}\ s^{-1}$, which are much higher than that of MoS_2 monolayer, but much smaller than that of Sc_2CO_2 due to defect scattering caused by sulfur vacancies. Therefore, Sc_2CS and Y_2CS with suitable carrier mobility and mechanical properties are promising as an excellent nanoelectronic materials. This work is expected to provide theoretical insights for the preparation and application of S-terminated MXenes and the discovery of novel MXene materials.

Conflicts of interest

The authors declare no competing financial interest.

Acknowledgements

The authors acknowledge the support of the Key R & D Projects of Zhejiang Province (No. 2022C01236, 2019C01060), the National Natural Science Foundations of China (Grant No. 52250005, 21875271, U20B2021, 21707147, 51372046, 51479037, 91226202, and 91426304), the Entrepreneurship Program of Foshan National Hi-tech Industrial Development Zone, the Major Project of the Ministry of Science and Technology of China (Grant No. 2015ZX06004-001), Ningbo Natural Science Foundations (Grant No. 2014A610006, 2016A610273, and 2019A610106).

References

1 D. Xiong, X. Li, Z. Bai and S. Lu, Recent Advances in Layered $Ti_3C_2T_x$ MXene for Electrochemical Energy Storage, *Small*, 2018, **14**(17), e1703419.
2 X. Xu, Y. Zhang, H. Sun, J. Zhou, F. Yang, H. Li, H. Chen, Y. Chen, Z. Liu, Z. Qiu, D. Wang, L. Ma, J. Wang, Q. Zeng and Z. Peng, Progress and Perspective: MXene and MXene-Based Nanomaterials for High-Performance Energy Storage Devices, *Adv. Electron. Mater.*, 2021, **7**(7), 2000967.
3 H. Kim and H. N. Alshareef, MXetronics: MXene-Enabled Electronic and Photonic Devices, *ACS Mater. Lett.*, 2019, **2**(1), 55–70.
4 S. Lee, E. H. Kim, S. Yu, H. Kim, C. Park, S. W. Lee, H. Han, W. Jin, K. Lee, C. E. Lee, J. Jang, C. M. Koo and C. Park, Polymer-Laminated $Ti_3C_2T_x$ MXene Electrodes for Transparent and Flexible Field-Driven Electronics, *ACS Nano*, 2021, **15**(5), 8940–8952.
5 E. Lee, A. VahidMohammadi, Y. S. Yoon, M. Beidaghi and D. J. Kim, Two-Dimensional Vanadium Carbide MXene for Gas Sensors with Ultrahigh Sensitivity Toward Nonpolar Gases, *ACS Sens.*, 2019, **4**, 1603–1611.
6 S. Mehdi Aghaei, A. Aasi and B. Panchapakesan, Experimental and Theoretical Advances in MXene-Based Gas Sensors, *ACS Omega*, 2021, **6**(4), 2450–2461.
7 Y. Li, Y. Chen, Z. Guo, C. Tang, B. Sa, N. Miao, J. Zhou and Z. Sun, Breaking the linear scaling relations in MXene catalysts for efficient CO_2 reduction, *Chem. Eng. J.*, 2022, **429**, 132171.
8 J. Yin, B. Ge, T. Jiao, Z. Qin, M. Yu, L. Zhang, Q. Zhang and Q. Peng, Self-Assembled Sandwich-like MXene-Derived Composites as Highly Efficient and Sustainable Catalysts for Wastewater Treatment, *Langmuir*, 2021, **37**(3), 1267–1278.
9 X. Zhan, C. Si, J. Zhou and Z. Sun, MXene and MXene-based composites: synthesis, properties and environment-related applications, *Nanoscale Horiz.*, 2020, **5**(2), 235–258.
10 S. Chertopalov and V. N. Mochalin, Environment-Sensitive Photoresponse of Spontaneously Partially Oxidized Ti(3)C(2) MXene Thin Films, *ACS Nano*, 2018, **12**(6), 6109–6116.
11 K. Huang, Z. Li, J. Lin, G. Han and P. Huang, Two-dimensional transition metal carbides and nitrides (MXenes) for biomedical applications, *Chem. Soc. Rev.*, 2018, **47**(14), 5109–5124.
12 M. Naguib, M. Kurtoglu, V. Presser, J. Lu, J. Niu, M. Heon, L. Hultman, Y. Gogotsi and M. W. Barsoum, Two-dimensional nanocrystals produced by exfoliation of Ti_3AlC_2, *Adv. Mater.*, 2011, **23**(37), 4248–4253.
13 B. Xu and Y. Gogotsi, MXenes-The fastest growing materials family in the two-dimensional world, *Chin. Chem. Lett.*, 2020, **31**(04), 919–921.

14 B. Anasori, M. R. Lukatskaya and Y. Gogotsi, 2D metal carbides and nitrides (MXenes) for energy storage, *Nat. Rev. Mater.*, 2017, **2**(2), 16098.

15 A. VahidMohammadi, J. Rosen and Y. Gogotsi, The world of two-dimensional carbides and nitrides (MXenes), *Science*, 2021, **372**(6547), 1165.

16 V. Kamysbayev, A. S. Filatov, H. Hu, X. Rui, F. Lagunas, D. Wang, R. F. Klie and D. V. Talapin, Covalent surface modifications and superconductivity of two-dimensional metal carbide MXenes, *Science*, 2020, **369**(6506), 979–983.

17 Y. Wei, P. Zhang, R. A. Soomro, Q. Zhu and B. Xu, Advances in the Synthesis of 2D MXenes, *Adv. Mater.*, 2021, **33**(39), e2103148.

18 M. Li, J. Lu, K. Luo, Y. Li, K. Chang, K. Chen, J. Zhou, J. Rosen, L. Hultman, P. Eklund, P. O. A. Persson, S. Du, Z. Chai, Z. Huang and Q. Huang, Element Replacement Approach by Reaction with Lewis Acidic Molten Salts to Synthesize Nanolaminated MAX Phases and MXenes, *J. Am. Chem. Soc.*, 2019, **141**(11), 4730–4737.

19 Y. Li, H. Shao, Z. Lin, J. Lu, L. Liu, B. Duployer, P. O. A. Persson, P. Eklund, L. Hultman, M. Li, K. Chen, X. H. Zha, S. Du, P. Rozier, Z. Chai, E. Raymundo-Pinero, P. L. Taberna, P. Simon and Q. Huang, A general Lewis acidic etching route for preparing MXenes with enhanced electrochemical performance in non-aqueous electrolyte, *Nat. Mater.*, 2020, **19**(8), 894–899.

20 H. Ding, Y. Li, M. Li, K. Chen, K. Liang, G. Chen, J. Lu, J. Palisaitis, P. O. Persson, P. Eklund, L. Hultman, S. Du, Z. Chai, Y. Gogotsi and Q. Huang, Chemical-scissor-mediated structural editing of layered transition metal carbides, *Science*, 2023, **379**(6637), 1130–1135.

21 T. Hu, Z. Li, M. Hu, J. Wang, Q. Hu, Q. Li and X. Wang, Chemical Origin of Termination-Functionalized MXenes: $Ti_3C_2T_2$ as a Case Study, *J. Phys. Chem. C*, 2017, **121**(35), 19254–19261.

22 X. Li, Z. Huang, C. E. Shuck, G. Liang, Y. Gogotsi and C. Zhi, MXene chemistry, electrochemistry and energy storage applications, *Nat. Rev. Chem.*, 2022, **6**(6), 389–404.

23 J. L. Hart, K. Hantanasirisakul, A. C. Lang, B. Anasori, D. Pinto, Y. Pivak, J. T. van Omme, S. J. May, Y. Gogotsi and M. L. Taheri, Control of MXenes' electronic properties through termination and intercalation, *Nat. Commun.*, 2019, **10**(1), 522.

24 X. Li, M. Li, Z. Huang, G. Liang, Z. Chen, Q. Yang, Q. Huang and C. Zhi, Activating the I^0/I^+ redox couple in an aqueous I_2–Zn battery to achieve a high voltage plateau, *Energy Environ. Sci.*, 2021, **14**(1), 407–413.

25 X. Liang, A. Garsuch and L. F. Nazar, Sulfur cathodes based on conductive MXene nanosheets for high-performance lithium-sulfur batteries, *Angew. Chem., Int. Ed.*, 2015, **54**(13), 3907–3911.

26 C. Wei, T. Fang, X. Tang, P. Wang and X. Liu, Non-Negligible Role of Multifunctional MXene Hosts for Li–S Batteries: Anchoring and Electrocatalysis, *J. Phys. Chem. C*, 2022, **126**(40), 17066–17075.

27 Y. Wang, J. Shen, L. C. Xu, Z. Yang, R. Li, R. Liu and X. Li, Sulfur-functionalized vanadium carbide MXene (V_2CS_2) as a promising anchoring material for lithium-sulfur batteries, *Phys. Chem. Chem. Phys.*, 2019, **21**(34), 18559–18568.

28 J. Zhu, A. Chroneos, J. Eppinger and U. Schwingenschlögl, S-functionalized MXenes as electrode materials for Li-ion batteries, *Appl. Mater. Today*, 2016, **5**, 19–24.

29 Q. Meng, J. Ma, Y. Zhang, Z. Li, C. Zhi, A. Hu and J. Fan, The S-functionalized Ti_3C_2 MXene as a high capacity electrode material for Na-ion batteries: a DFT study, *Nanoscale*, 2018, **10**(7), 3385–3392.

30 V. Shukla, N. K. Jena, S. R. Naqvi, W. Luo and R. Ahuja, Modelling high-performing batteries with Mxenes: The case of S-functionalized two-dimensional nitride MXene electrode, *Nano Energy*, 2019, **58**, 877–885.

31 L. Zhang, W. Zhang, X. Ma, X. Zhang and J. Wen, Computational screening of functionalized MXenes to catalyze the solid and non-solid conversion reactions in cathodes of lithium-sulfur batteries, *Phys. Chem. Chem. Phys.*, 2022, **24**(15), 8913–8922.

32 Z. Li, Y. Wu and J. Hou, Exploring the anchoring effect of surface functionalized 2D electrodes Ca_2N and Y_2C in lithium sulfur battery: First principle study, *Appl. Surf. Sci.*, 2022, **591**, 153185.

33 S. Wang, Y. Wang, Q. Zhou, X. Li, Y. Li, Y. Liu, Y. Sun, T. Wang, L. C. Xu and Y. Wang, Modelling high performance potassium-ion battery anode materials with two-dimensional vanadium carbide MXene: the role of surface O- and S-terminations, *Phys. Chem. Chem. Phys.*, 2021, **23**(6), 3898–3904.

34 K. A. Papadopoulou, A. Chroneos and S.-R. G. Christopoulos, Mg-ion diffusion on the surface of $Ti_3C_2S_2$ MXene, *J. Phys. Chem. Solids*, 2022, **166**, 110713.

35 S.-P. Huang, J.-F. Gu, Y.-R. Ren, K.-N. Ding, Y. Li, Y.-F. Zhang, S.-P. Huang, W. Lin and W.-K. Chen, Investigation of Ordered TiMC and $TiMCT_2$ (M = Cr and Mo; T = O and S) MXenes as High-Performance Anode Materials for Lithium-Ion Batteries, *J. Phys. Chem. C*, 2022, **126**(11), 5283–5291.

36 G. Chaney, D. Cakir, F. M. Peeters and C. Ataca, Stability of adsorption of Mg and Na on sulfur-functionalized MXenes, *Phys. Chem. Chem. Phys.*, 2021, **23**(44), 25424–25433.

37 Z. Chen, S. Huang, X. Yuan, X. Gan and N. Zhou, A comparative study of M_2CS_2 and M_2CO_2 MXenes as anode materials for lithium ion batteries, *Appl. Surf. Sci.*, 2021, **544**, 148861.

38 H. Luo, X. Wang, C. Wan, L. Xie, M. Song and P. Qian, A Theoretical Study of Fe Adsorbed on Pure and Nonmetal (N, F, P, S, Cl)-Doped $Ti_3C_2O_2$ for Electrocatalytic Nitrogen Reduction, *Nanomaterials*, 2022, **12**(7), 1081.

39 S. Bae, W. Espinosa-García, Y. G. Kang, *et al.*, MXene Phase with C3 Structure Unit: A Family of 2D Electrodes, *Adv. Funct. Mater.*, 2021, **31**(24), 2100009.

40 Z. Wang, N. Qiu, E. Wu, Q. Huang, P. An, H. He and S. Du, First-principles study of electronic and optical properties of NH_3-adsorbed Sc_2CO_2 monolayer and its application in gas sensors, *J. Mater. Res. Technol.*, 2023, **24**, 173–184.

41 C. Hu, X. Yu, Y. Li, J. Cheng and B. Xiao, M_2CS_2 (M = Sc, Y) with brand-new MXene phase: The promising candidate as the N/O-containing gases sensor and/or capturer, *Appl. Surf. Sci.*, 2023, **607**, 155104.

42 L. Zhang, C. Tang, C. Zhang and A. Du, First-principles screening of novel ferroelectric MXene phases with a large piezoelectric response and unusual auxeticity, *Nanoscale*, 2020, **12**(41), 21291–21298.

43 E. M. D. Siriwardane, I. Demiroglu, C. Sevik, F. M. Peeters and D. Çakır, Assessment of Sulfur-Functionalized MXenes for Li-Ion Battery Applications, *J. Phys. Chem. C*, 2020, **124**(39), 21293–21304.

44 Y. Jing, J. Liu, Z. Zhou, J. Zhang and Y. Li, Metallic Nb_2S_2C Monolayer: A Promising Two-Dimensional Anode Material for Metal-Ion Batteries, *J. Phys. Chem. C*, 2019, **123**(44), 26803–26811.

45 X. Liu, X. Shao, F. Li and M. Zhao, Anchoring effects of S-terminated Ti_2C MXene for lithium-sulfur batteries: A first-principles study, *Appl. Surf. Sci.*, 2018, **455**, 522–526.

46 V. Mehta, H. S. Saini, S. Srivastava, M. K. Kashyap and K. Tankeshwar, S-Functionalized Mo_2C Monolayer as a Novel Electrode Material in Li-Ion Batteries, *J. Phys. Chem. C*, 2019, **123**(41), 25052–25060.

47 Y. Li, L. Bai, N. Ma and L. Niu, O- or/and S-functionalized Cr_2C as electrode material for metal-ion (Li, Na, K, and Mg) batteries: A first principles study, *Comput. Theor. Chem.*, 2022, **1217**, 113892.

48 J. Yang, A. Wang, S. Zhang, H. Wu and L. Chen, Stability and electronic properties of sulfur terminated two-dimensional early transition metal carbides and nitrides (MXene), *Comput. Mater. Sci.*, 2018, **153**, 303–308.

49 S. Lee, S. C. Jung and Y. K. Han, Fe_2CS_2 MXene: a promising electrode for Al-ion batteries, *Nanoscale*, 2020, **12**(9), 5324–5331.

50 G. Kresse and D. Joubert, From ultrasoft pseudopotentials to the projector augmented-wave method, *Phys. Rev. B: Condens. Matter Mater. Phys.*, 1999, **59**(3), 1758–1775.

51 J. P. Perdew, K. Burke and M. Ernzerhof, Generalized Gradient Approximation Made Simple, *Phys. Rev. Lett.*, 1996, **77**(18), 3865–3868.

52 E. Caldeweyher, C. Bannwarth and S. Grimme, Extension of the D3 dispersion coefficient model, *J. Chem. Phys.*, 2017, **147**(3), 034112.

53 A. Togo and I. Tanaka, First principles phonon calculations in materials science, *Scr. Mater.*, 2015, **108**, 1–5.

54 X. Gonze and C. Lee, Dynamical matrices, Born effective charges, dielectric permittivity tensors, and interatomic force constants from density-functional perturbation theory, *Phys. Rev. B: Condens. Matter Mater. Phys.*, 1997, **55**(16), 10355–10368.

55 J. P. Perdew and M. Levy, Physical Content of the Exact Kohn-Sham Orbital Energies: Band Gaps and Derivative Discontinuities, *Phys. Rev. Lett.*, 1983, **51**(20), 1884–1887.

56 J. Liu, X.-B. Li, D. Wang, H. Liu, P. Peng and L.-M. Liu, Single-layer Group-IVB nitride halides as promising photocatalysts, *J. Mater. Chem. A*, 2014, **2**(19), 6755.

57 M. C. Toroker, D. K. Kanan, N. Alidoust, L. Y. Isseroff, P. Liao and E. A. Carter, First principles scheme to evaluate band edge positions in potential transition metal oxide photocatalysts and photoelectrodes, *Phys. Chem. Chem. Phys.*, 2011, **13**(37), 16644–16654.

58 A. K. Singh, K. Mathew, H. L. Zhuang and R. G. Hennig, Computational Screening of 2D Materials for Photocatalysis, *J. Phys. Chem. Lett.*, 2015, **6**(6), 1087–1098.

59 J. Dai and X. C. Zeng, Titanium trisulfide monolayer: theoretical prediction of a new direct-gap semiconductor with high and anisotropic carrier mobility, *Angew. Chem., Int. Ed. Engl.*, 2015, **54**(26), 7572–7576.

60 J. Bardeen and W. Shockley, Deformation Potentials and Mobilities in Non-Polar Crystals, *Phys. Rev.*, 1950, **80**(1), 72–80.

61 K. Momma and F. Izumi, VESTA 3 for three-dimensional visualization of crystal, volumetric and morphology data, *J. Appl. Crystallogr.*, 2011, **44**(6), 1272–1276.

62 B. Xiao, Y.-c. Li, X.-f. Yu and J.-b. Cheng, MXenes: Reusable materials for NH_3 sensor or capturer by controlling the charge injection, *Sens. Actuators, B*, 2016, **235**, 103–109.

63 F. Zhang, H. Zhang, S. Krylyuk, C. A. Milligan, Y. Zhu, D. Y. Zemlyanov, L. A. Bendersky, B. P. Burton, A. V. Davydov and J. Appenzeller, Electric-field induced structural transition in vertical $MoTe_2$- and $Mo_{1-x}W_xTe_2$-based resistive memories, *Nat. Mater.*, 2019, **18**(1), 55–61.

64 J.-C. Lian, H.-Y. Wu, W.-Q. Huang, W. Hu and G.-F. Huang, Algorithm for generating irreducible site-occupancy configurations, *Phys. Rev. B: Condens. Matter Mater. Phys.*, 2020, **102**, 134209.

65 K. Xiong, P. Wang, G. Yang, Z. Liu, H. Zhang, S. Jin and X. Xu, Functional Group Effects on the Photoelectronic Properties of MXene (Sc_2CT_2, T = O, F, OH) and Their Possible Photocatalytic Activities, *Sci. Rep.*, 2017, **7**(1), 15095.

66 Y. Jiang, Y. Zhang, Q. Huang, L. Hao and S. Du, The compositional dependence of structural stability and resulting properties for $M_{n+1}C_nT_2$ (M = Sc, Ti, V; T = O, OH, F, Cl, Br and I; n = 1, 2): first-principle investigations, *J. Mater. Res. Technol.*, 2020, **9**(6), 14979–14989.

67 S. Ma, D. Yuan, Z. Jiao, T. Wang and X. Dai, Monolayer Sc_2CO_2: A Promising Candidate as a SO_2 Gas Sensor or Capturer, *J. Phys. Chem. C*, 2017, **121**(43), 24077–24084.

68 M. Li, O. Omisakin and J. Young, Effect of chemical substitution and external strain on phase stability and ferroelectricity in two dimensional M_2CT_2 MXenes, *Nanoscale*, 2022, **14**(18), 6970–6980.

69 J. Young and T. L. Reinecke, Controlling the H to T' structural phase transition *via* chalcogen substitution in MoTe(2) monolayers, *Phys. Chem. Chem. Phys.*, 2017, **19**(47), 31874–31882.

70 V. Wang, G. Tang, Y. C. Liu, R. T. Wang, H. Mizuseki, Y. Kawazoe, J. Nara and W. T. Geng, High-Throughput Computational Screening of Two-Dimensional Semiconductors, *J. Phys. Chem. Lett.*, 2022, **13**(50), 11581–11594.

71 S. Chen, Z. Fu, H. Zhang, D. Legut, T. C. Germann, Q. Zhang, S. Du, J. S. Francisco and R. Zhang, Surface Electrochemical

Stability and Strain-Tunable Lithium Storage of Highly Flexible 2D Transition Metal Carbides, *Adv. Funct. Mater.*, 2018, **28**(44), 1804867.

72 M. Marsman, J. Paier, A. Stroppa and G. Kresse, Hybrid functionals applied to extended systems, *J. Phys.: Condens. Matter*, 2008, **20**(6), 064201.

73 V. L. Deringer, A. L. Tchougreeff and R. Dronskowski, Crystal orbital Hamilton population (COHP) analysis as projected from plane-wave basis sets, *J. Phys. Chem. A*, 2011, **115**(21), 5461–5466.

74 Z. Fu, D. Legut, T. C. Germann, C. Si, S. Du, J. S. Francisco and R. Zhang, Phonon-mediated stabilization and softening of 2D transition metal carbides: case studies of Ti_2CO_2 and Mo_2CO_2, *Phys. Chem. Chem. Phys.*, 2018, **20**(21), 14608–14618.

75 F. Mouhat and F.-X. Coudert, Necessary and sufficient elastic stability conditions in various crystal systems, *Phys. Rev. B: Condens. Matter Mater. Phys.*, 2014, **90**, 224104.

76 Z.-Y. Wang, Y.-L. Zhou, X.-Q. Wang, F. Wang, Q. Sun, Z.-X. Guo and Y. Jia, Effects of in-plane stiffness and charge transfer on thermal expansion of monolayer transition metal dichalcogenide, *Chin. Phys. B*, 2015, **24**(2), 026501.

77 Y. Cai, G. Zhang and Y.-W. Zhang, Polarity-Reversed Robust Carrier Mobility in Monolayer MoS_2 Nanoribbons, *J. Am. Chem. Soc.*, 2014, **136**(17), 6269–6275.